Electronic Supplementary Material (ESI) for RSC Advances.

Oxovanadium(IV) catecholates of terpyridine bases for cellular imaging and photocytotoxicity in red light

Bhabatosh Banik,[a] Kumar Somyajit,[b] Ganesh Nagaraju,*[b] and Akhil R. Chakravarty*[a]

Supporting Information

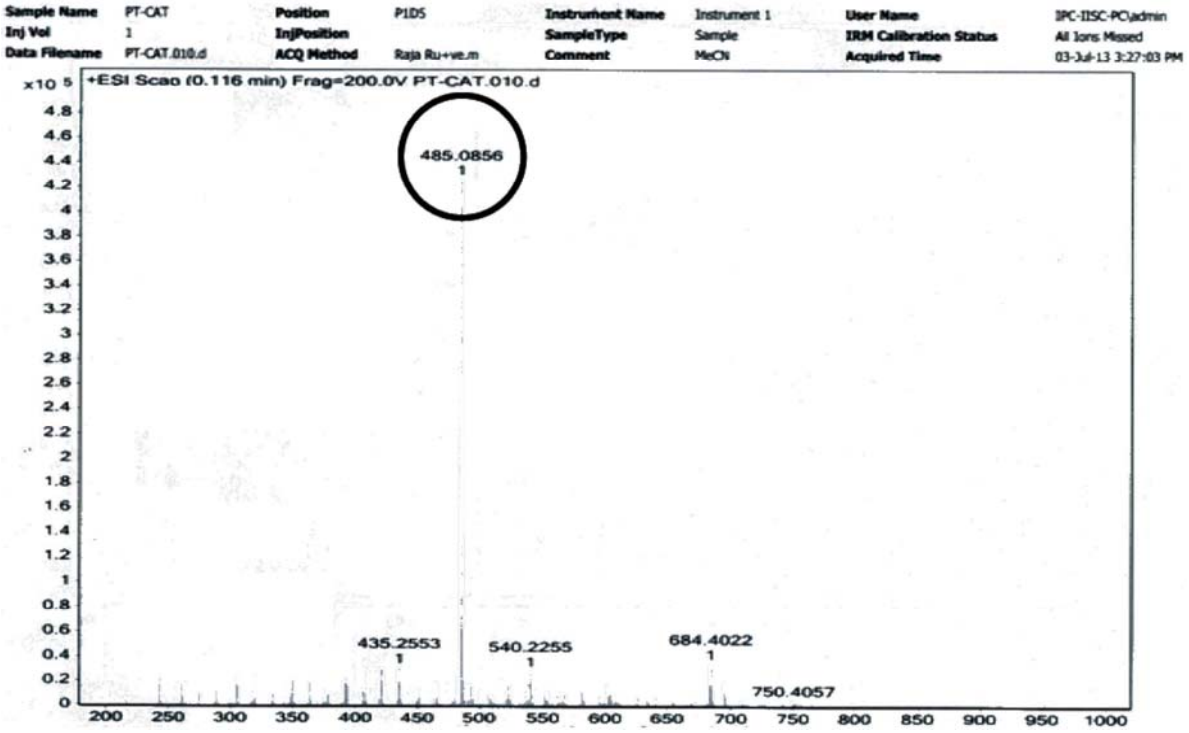

Fig. S1. The ESI-MS spectrum of complex **1** in MeCN showing the peak at 485.0856 that corresponds to $[M+H]^+$.

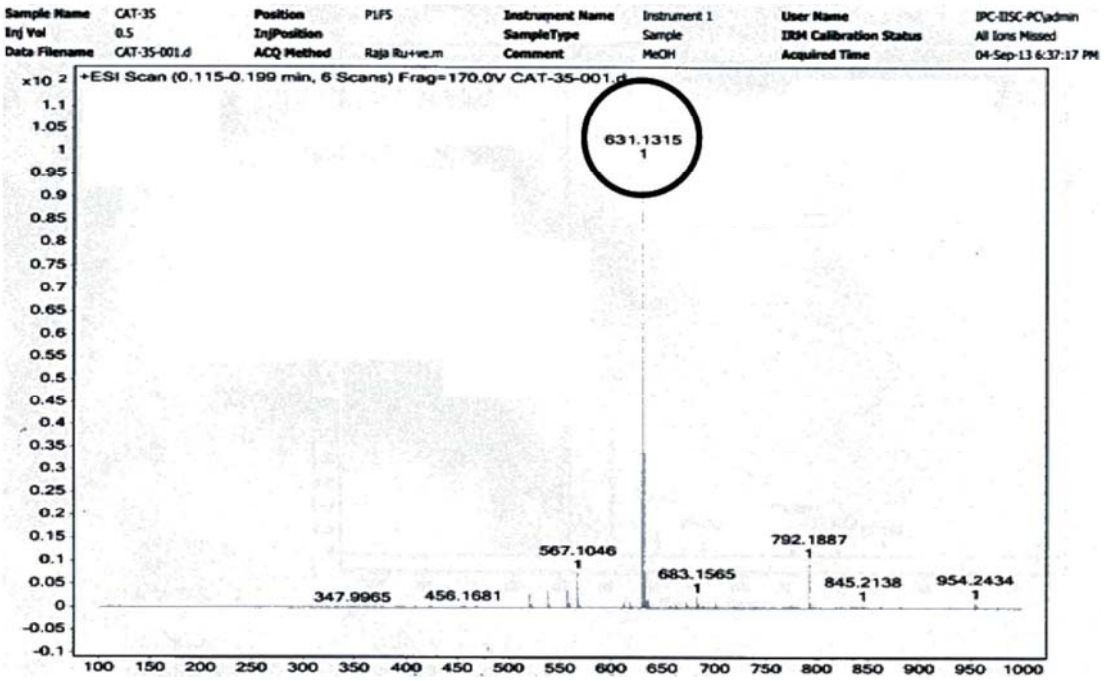

Fig. S2. The ESI-MS spectrum of complex **1** in MeCN showing the peak at 631.1315 that corresponds to $[M+H]^+$.

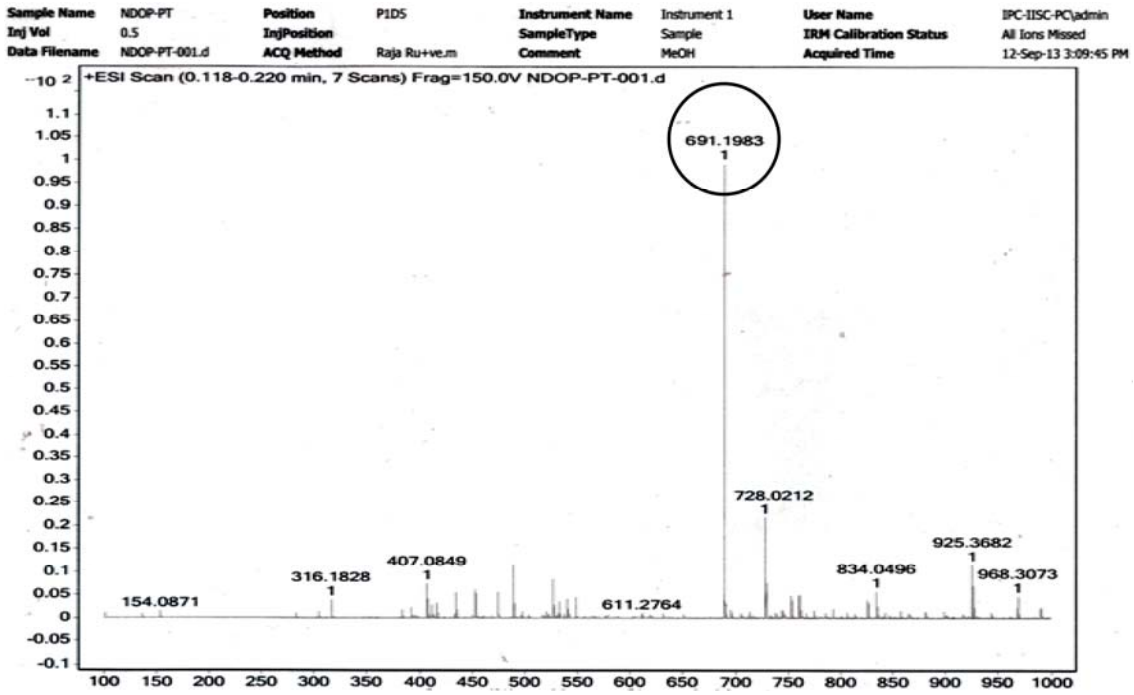

Fig. S3. The ESI-MS spectrum of complex **1** in MeCN showing the peak at 691.1983 that corresponds to $[M+H]^+$.

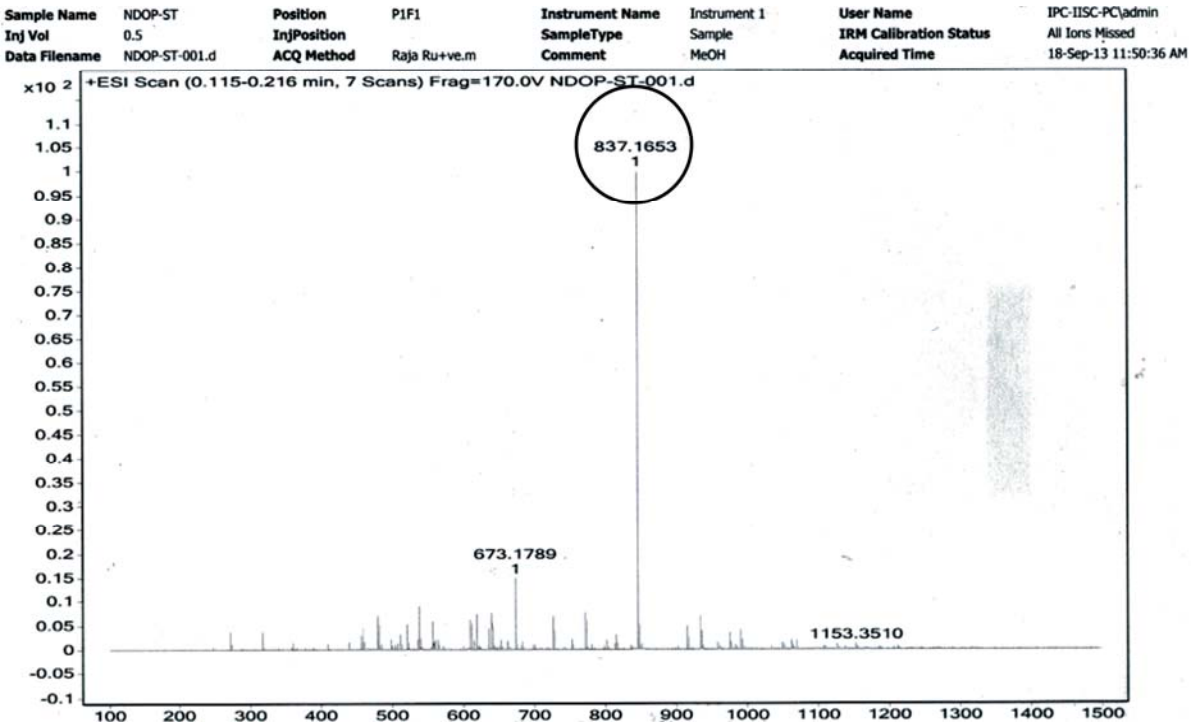

Fig. S4. The ESI-MS spectrum of complex **1** in MeCN showing the peak at 837.1653 that corresponds to $[M+H]^+$.

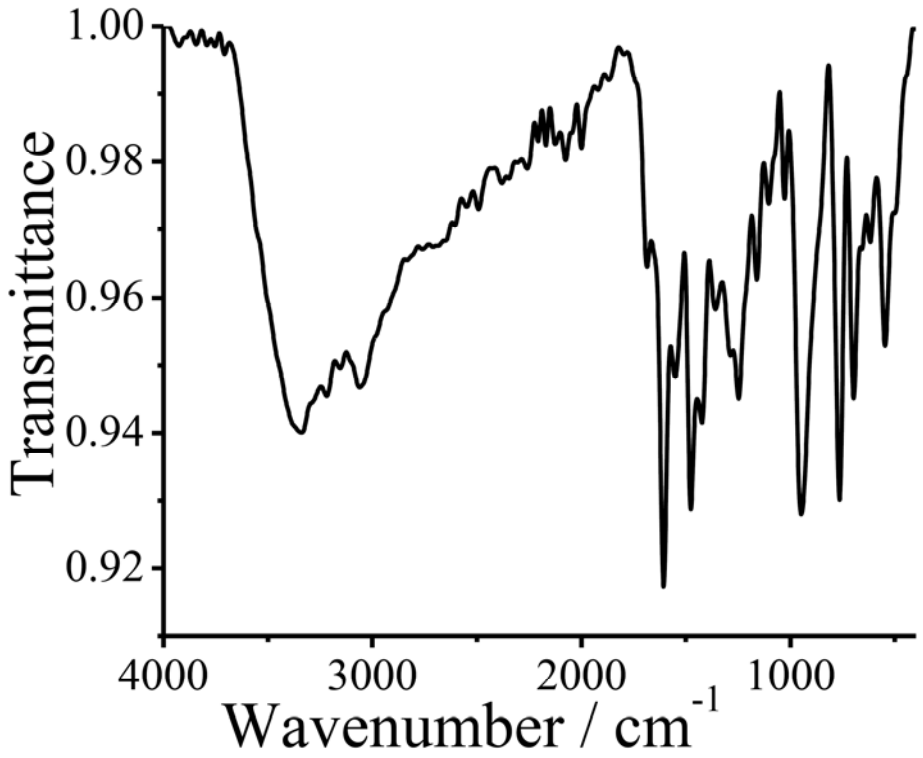

Fig. S5. IR spectrum of complex **1**.

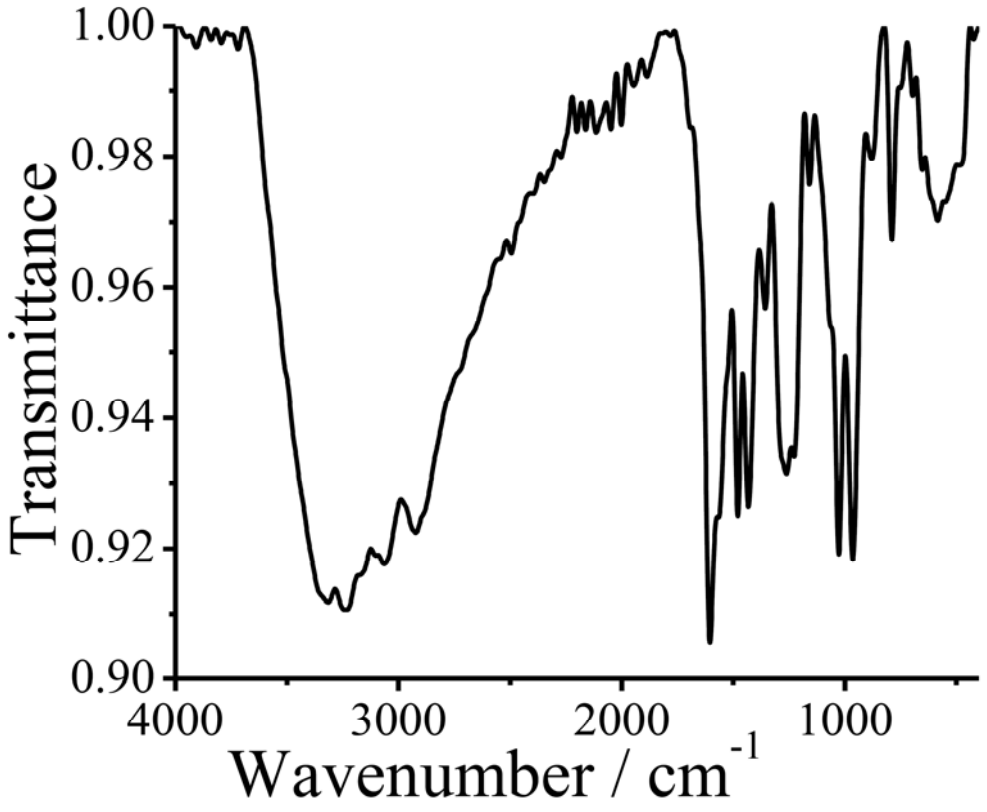

Fig. S6. IR spectrum of complex **2**.

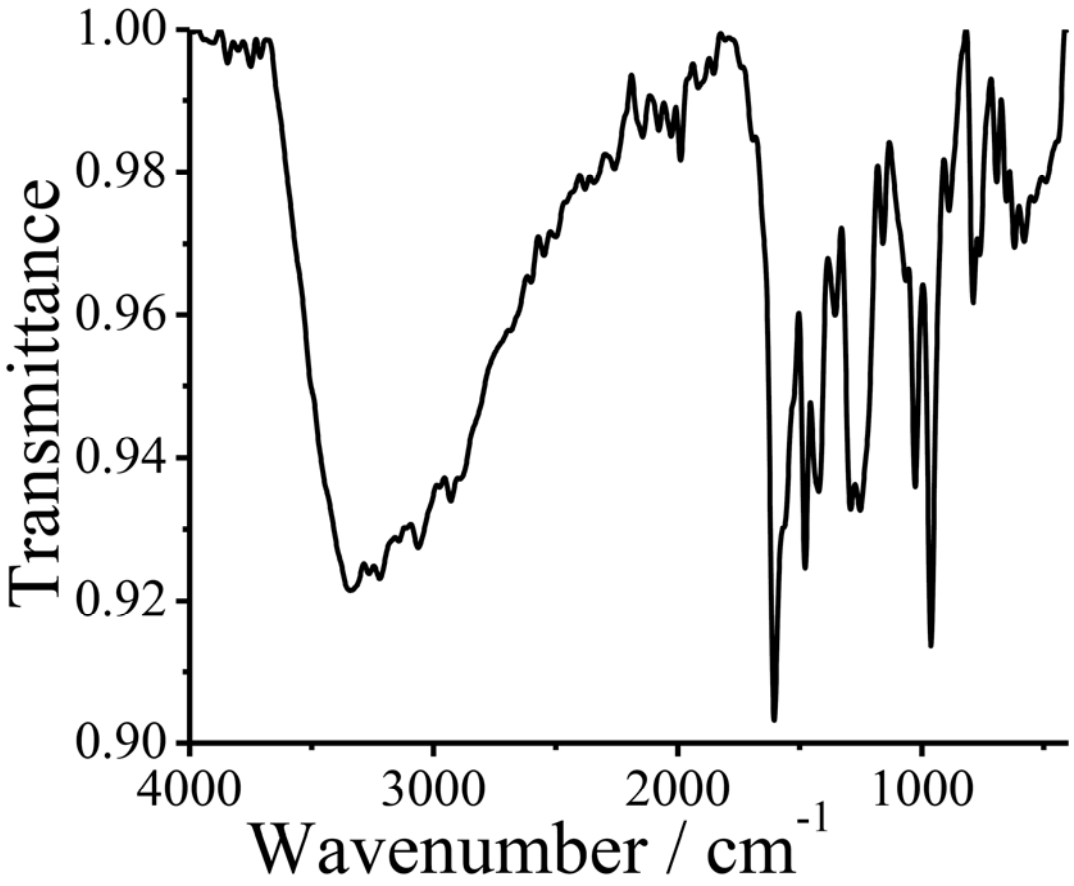

Fig. S7. IR spectrum of complex **3**.

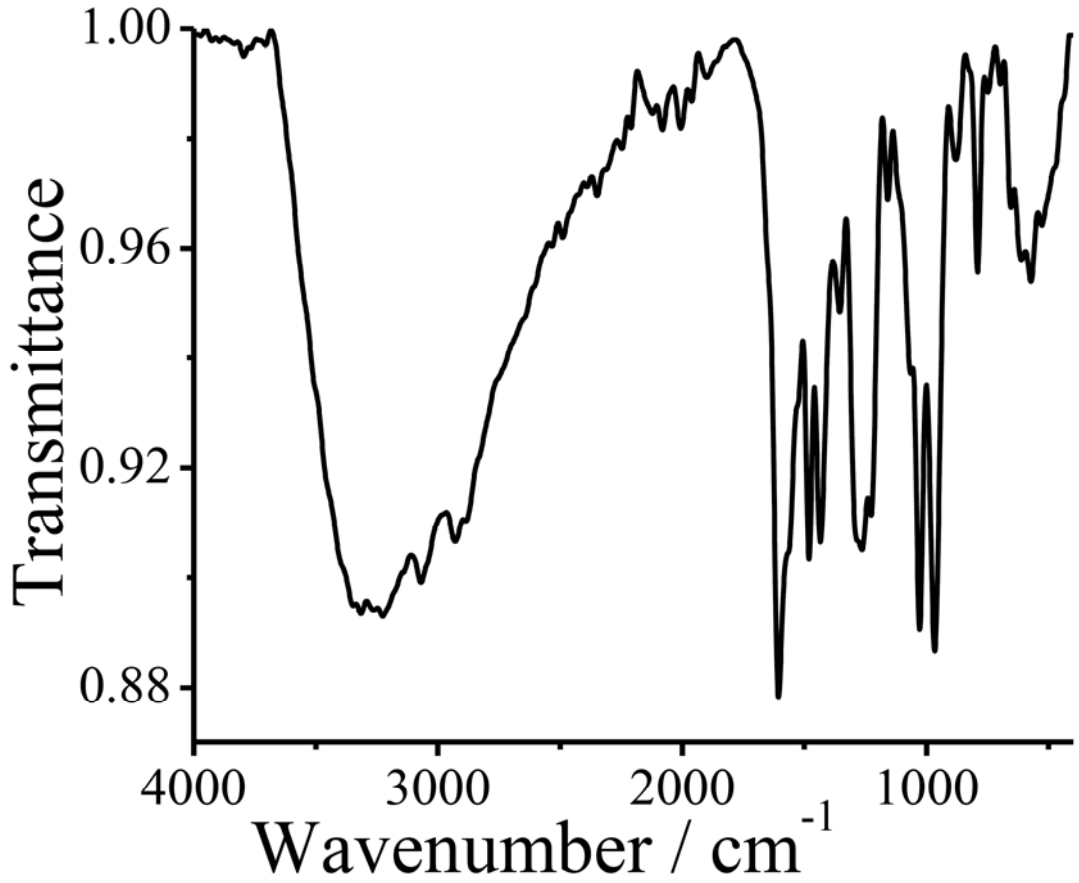

Fig. S8. IR spectrum of complex **4**.

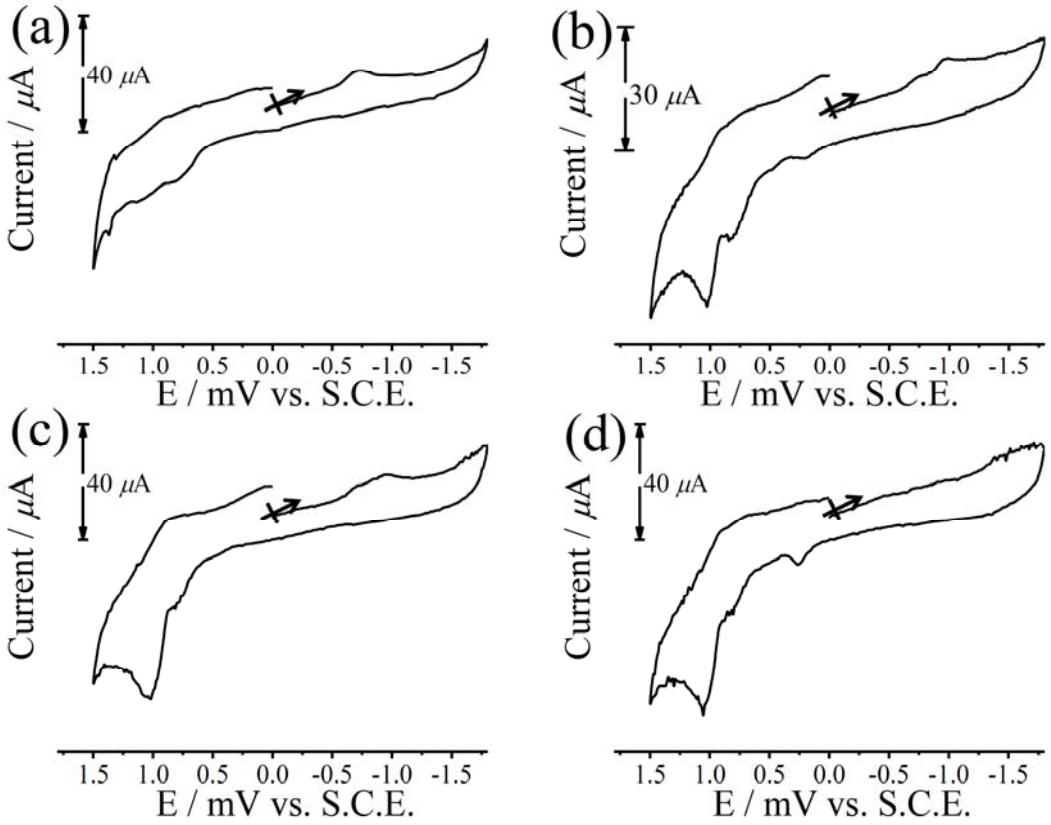

Fig. S9. Cyclic voltammograms of the complexes **1** (a), **2** (b), **3** (c) and **4** (d) in DMF at a scan speed of 50 mV s^{-1} and 0.1 M TBAP as a supporting electrolyte. The V(IV)-V(III) response is irreversible in nature showing only the cathodic peak without having any anodic counterpart. The oxidative response of the metal [V(V)-V(IV) couple] is near +1.0 V.

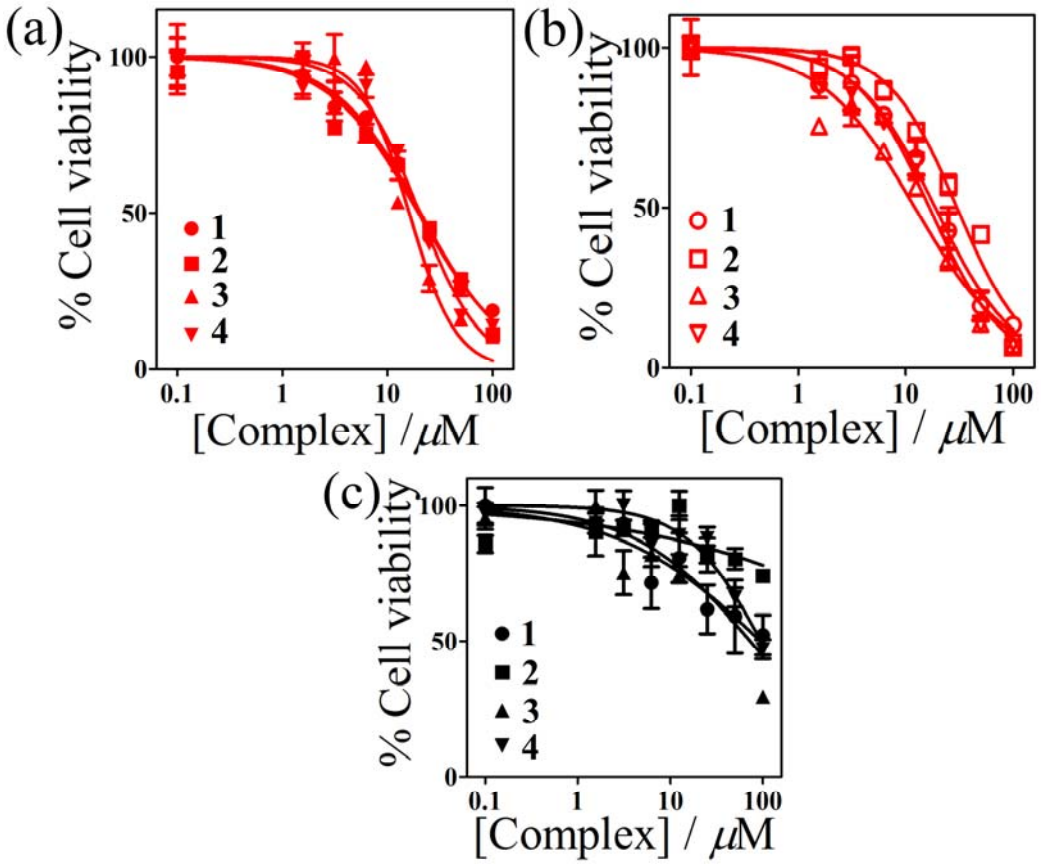

Fig. S10. Cell viability plots showing the cytotoxic effect of the complexes **1-4** in (a) red light (600-720 nm, 150 *J* cm^{-2}), (b) in visible light (400-700 nm, 10 *J* cm^{-2}) and (c) in dark in HeLa cells.

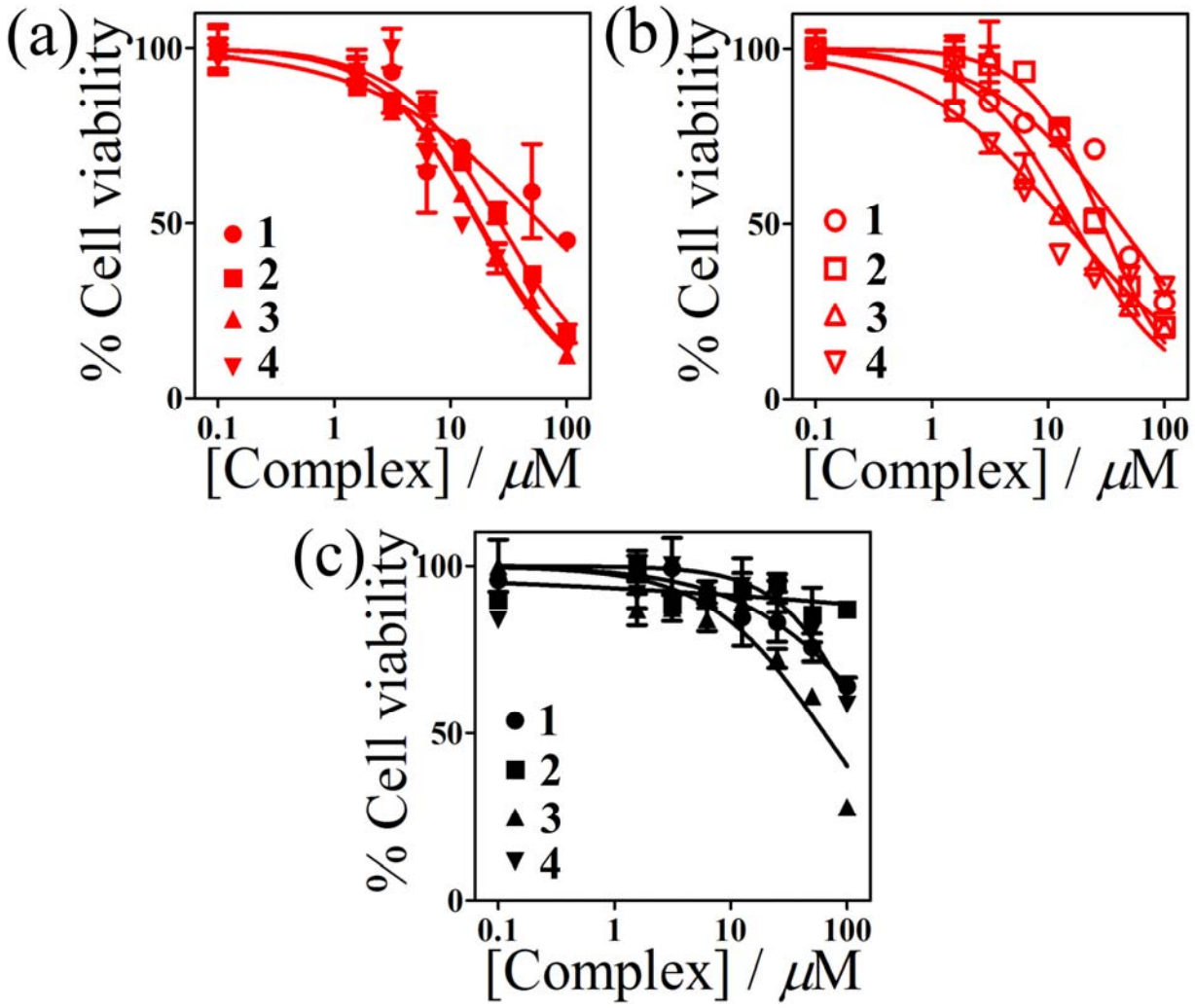

Fig. S11. Cell viability plots showing the cytotoxic effect of the complexes **1**-**4** (a) in red light (600-720 nm, 150 *J* cm^{-2}), (b) in visible light (400-700 nm, 10 *J* cm^{-2}) and (c) in dark in Hep G2 cells.

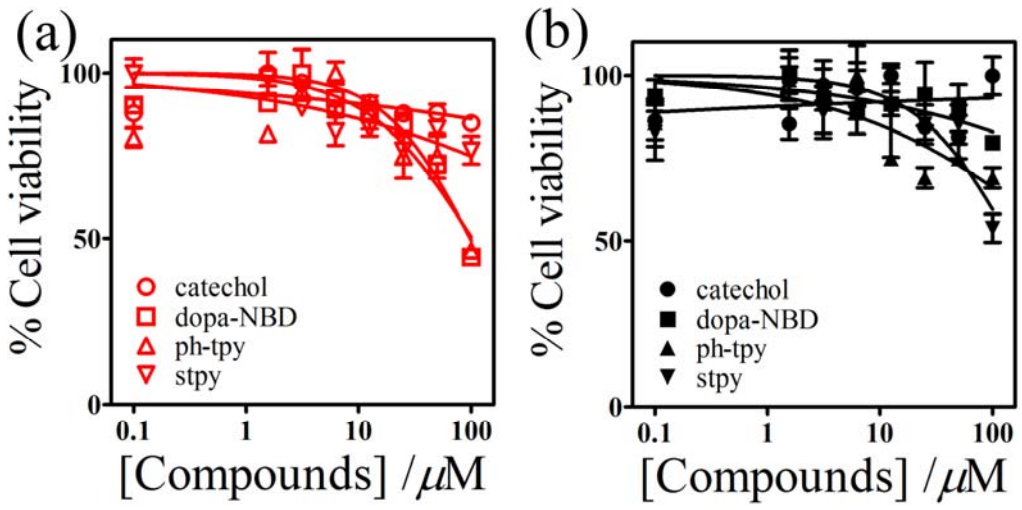

Fig. S12. Cell viability plots showing the cytotoxic effect of the ligands in (a) red light (600-720 nm, 150 *J* cm^{-2}) and (b) dark in HeLa cells.

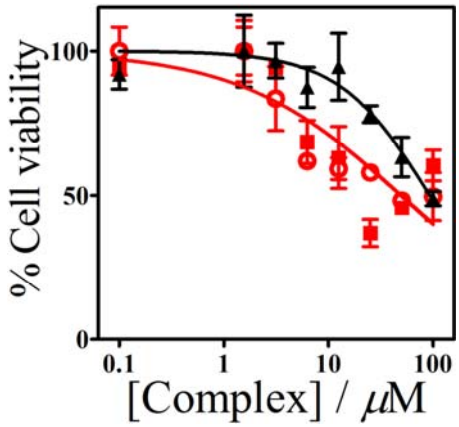

Fig. S13. Cell viability plots showing the cytotoxic effect of complex **4** in (■) red light (600-720 nm, 150 *J* cm^{-2}), (○) visible light (600-720 nm, 150 *J* cm^{-2}) and (▲) dark in HBL-100 cells giving IC50 values of 50.0 μM, 48.7 μM and 93.0 μM respectively.

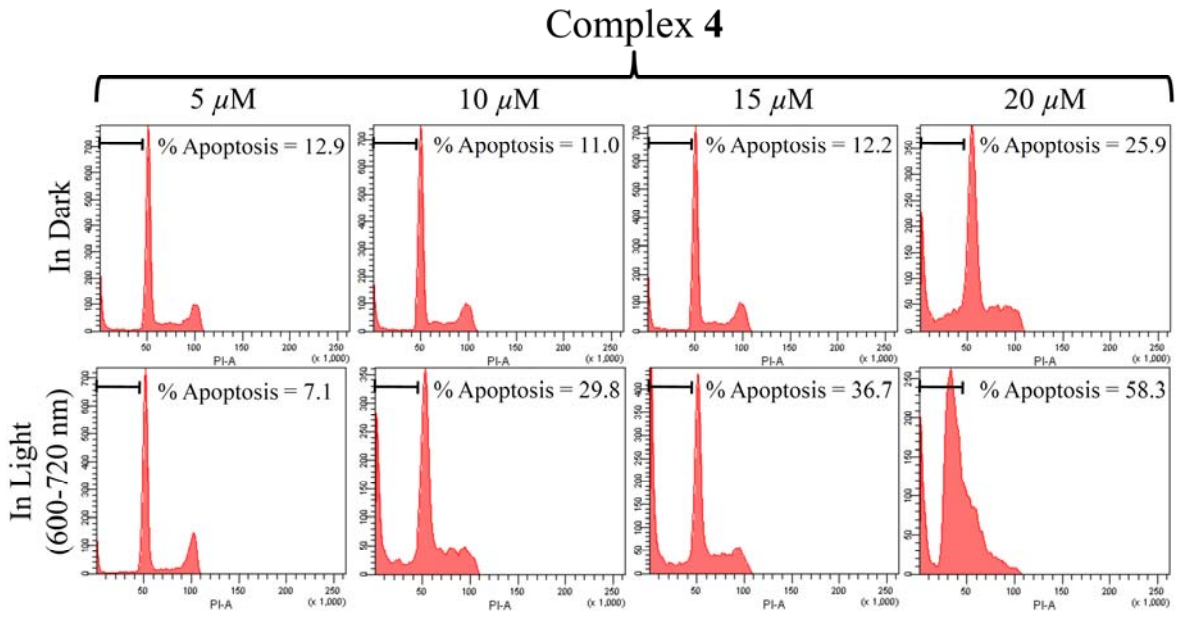

Fig. S14. Flow cytometric analysis of the apoptotic cell death induced by complex **4** at various concentrations in dark and red light (600-720 nm, 150 *J* cm^{-2}).

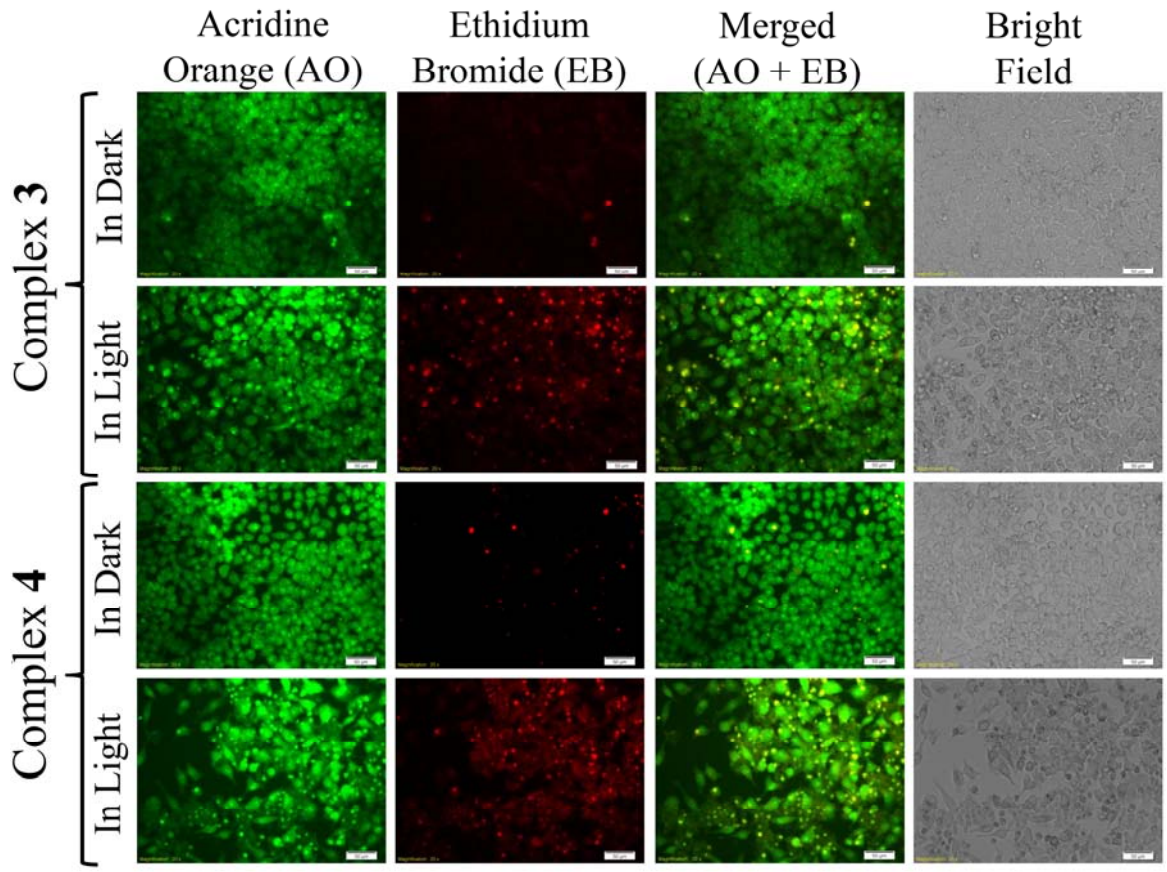

Fig. S15. Acridine orange / ethidium bromide (AO/EB) dual staining of HeLa cells treated with complexes **3** and **4** (10 µmol) to study the changes in nuclear morphology upon irradiation with red light (600-720 nm, 150 J cm^{-2}) after 6 h of incubation. The scale bar corresponds to 50 μm.

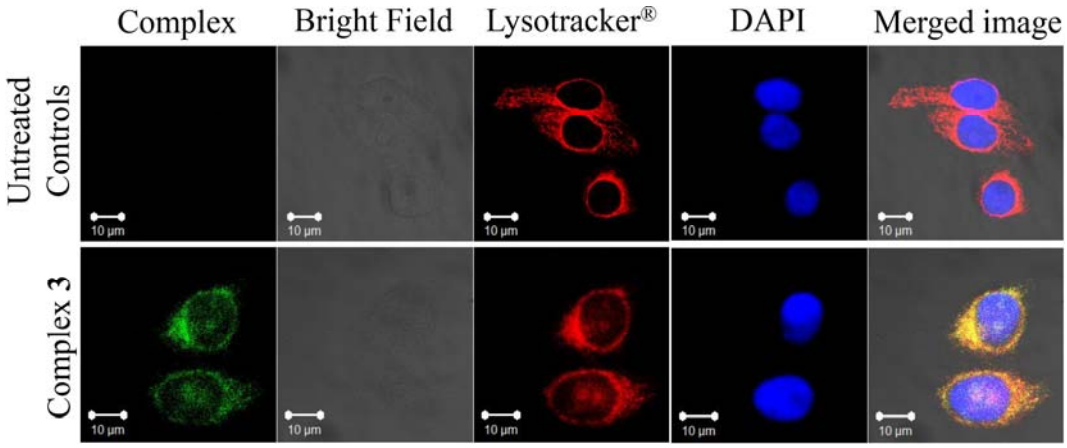

Fig. S16. Confocal microscopy images of complex **3** in HeLa cells showing co-localization with lysosomes of the cells. Scale bar: 10 µm.

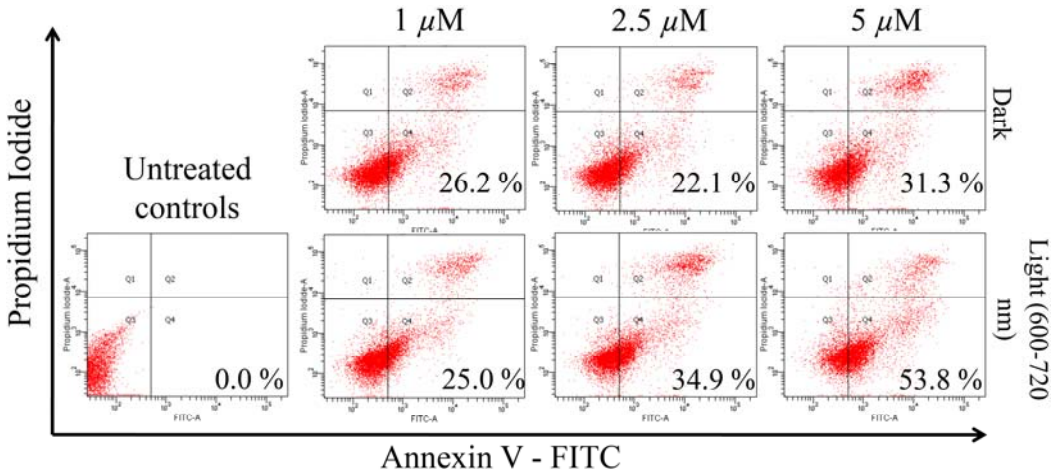

Fig. S17. Apoptosis inducing property of complex **4** by annexin V-FITC/PI staining of HeLa cells. Four distinct phenotypes: viable cells (lower left quadrant Q3); cells at an early stage of apoptosis (lower right quadrant Q4); cells at a late stage of apoptosis (upper right quadrant Q2); necrosis (upper left quadrant Q1).

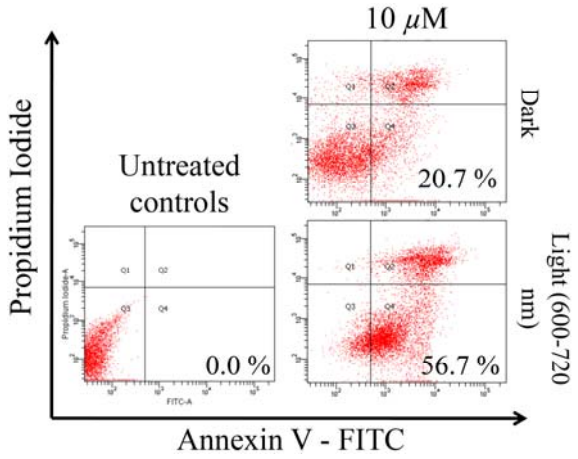

Fig. S18. Apoptosis inducing property of complex **4** (10 μM) by annexin V-FITC/PI staining of HeLa cells.

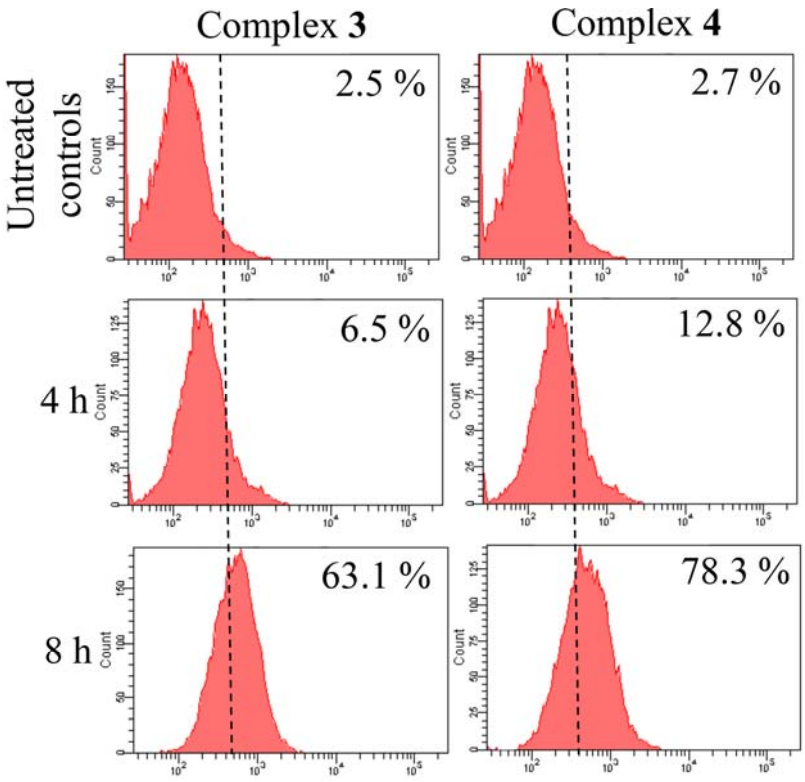

Fig. S19. Histograms showing cellular uptake of complexes **3** and **4** (5 μM) at various time points of incubation with HeLa cells as determined from the flow cytometric analysis.

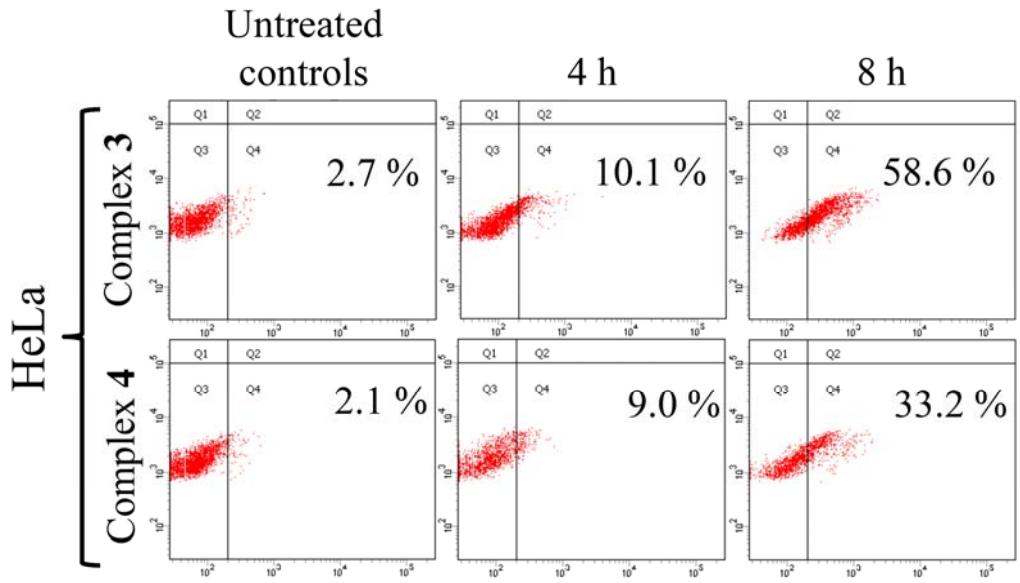

Fig. S20. Dot plots showing cellular uptake of complexes **3** and **4** (5 μM) at various time points of incubation with HeLa cells in glucose saturated media as determined from the flow cytometric analysis.

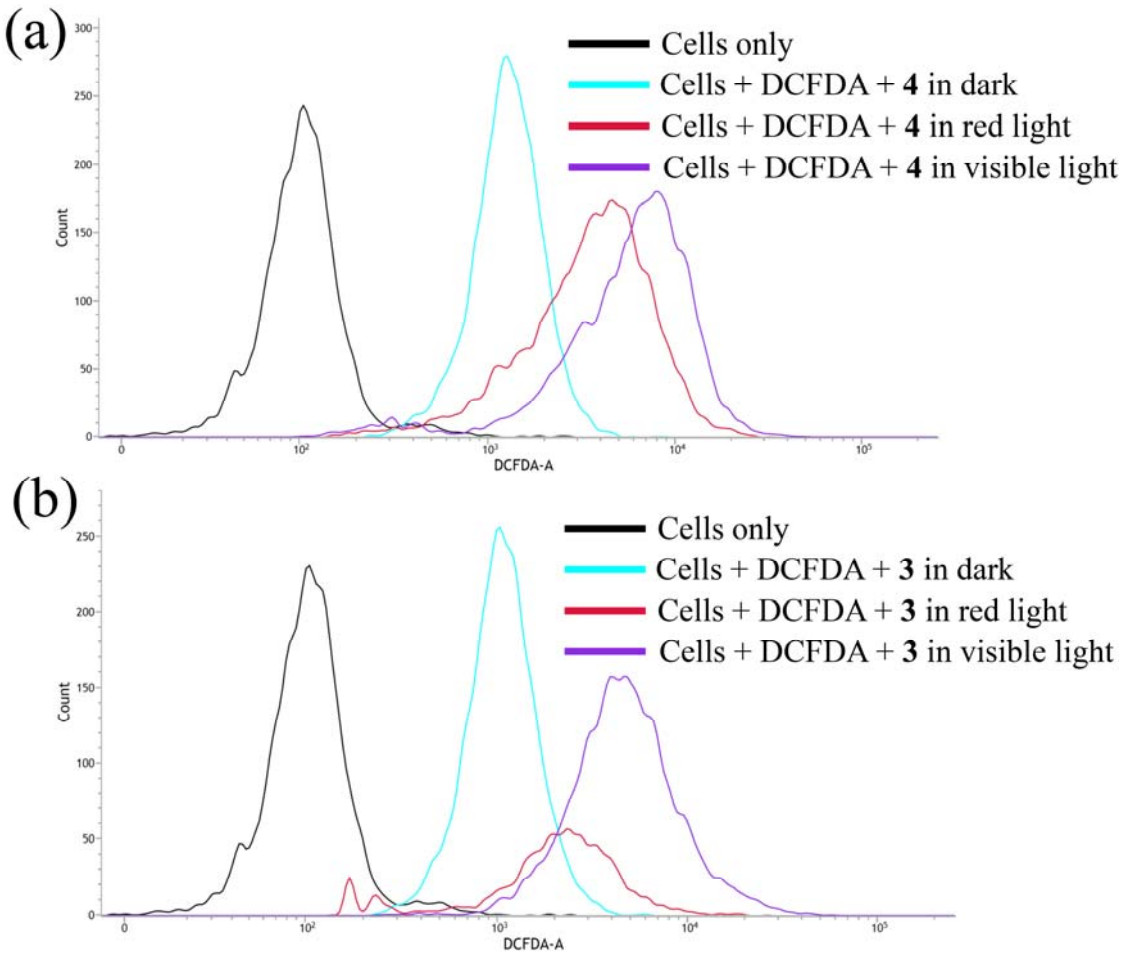

Fig. S21. Histograms showing the shift in the fluorescence intensity compared to that of only cells with addition of different additives as mentioned in the figure as determined by FACS studies. Greater shift implies higher fluorescence intensity resulting from higher amount of DCF formation and thus greater ROS generation.

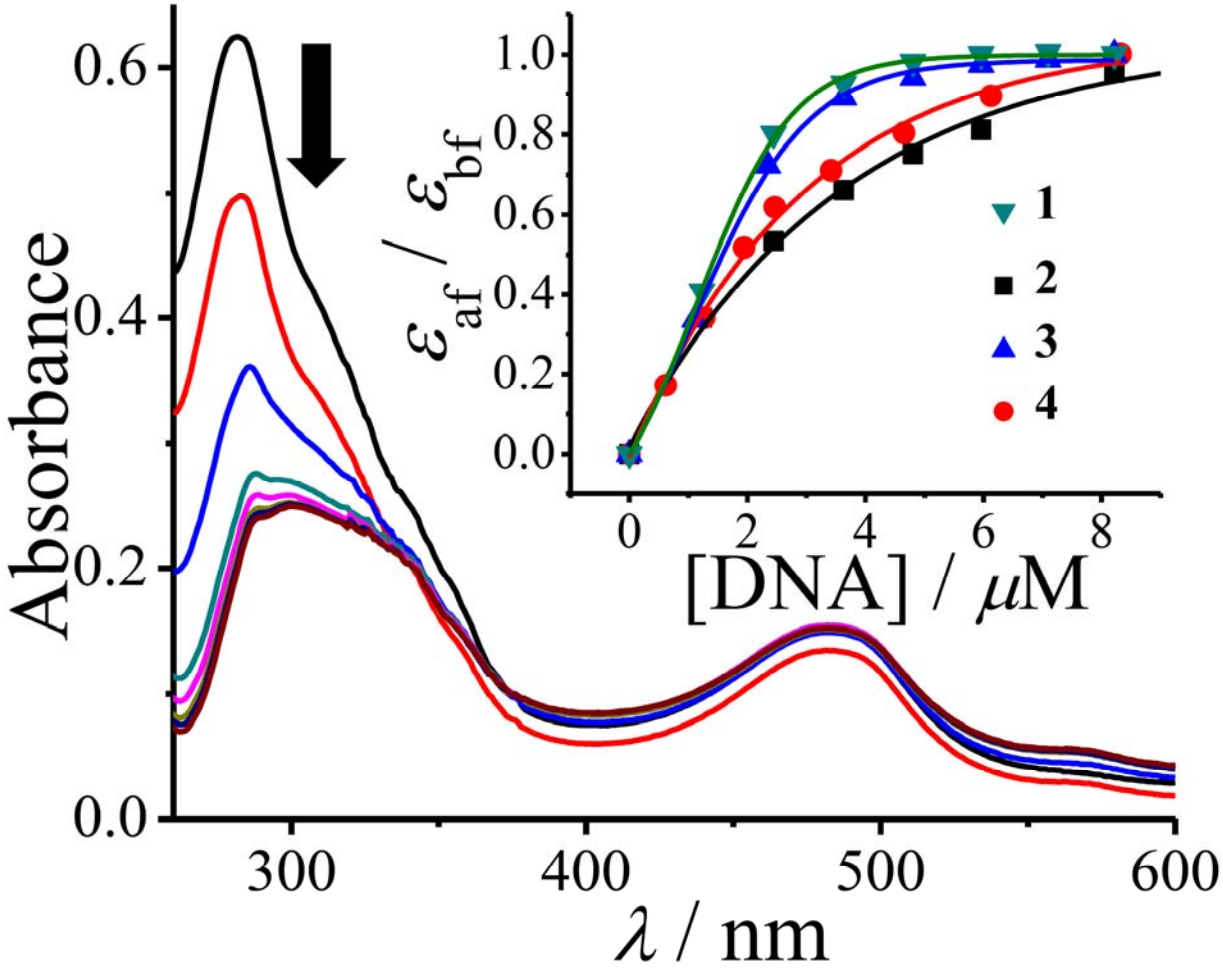

Fig. S22. Absorption spectral traces of [VO(dopa-NBD)(stpy)] (**3**) in 5 mM Tris-HCl buffer (pH 7.2) on increasing the quantity of ct-DNA (shown by arrow). Inset shows the least-squares fit of $\Delta\varepsilon_{af}/\Delta\varepsilon_{bf}$ vs. [DNA] for the complexes [VO(cat)(phtpy)] (**1**) (▼), [VO(cat)(stpy)] (**2**) (■), [VO(dopa-NBD)(phtpy)] (**3**) (▲) and [VO(dopa-NBD)(stpy)] (**4**) (●).

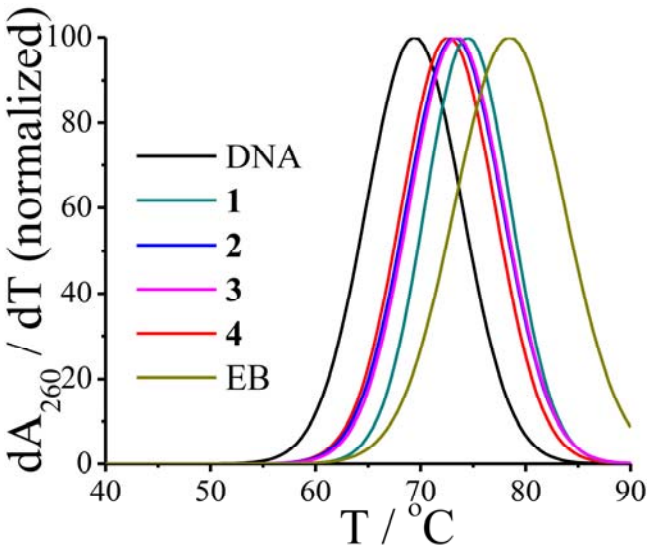

Fig. S23. Thermal denaturation plots of 150 μmol ct-DNA alone and in the presence of the complexes **1**-**4** and ethidium bromide (EB) at 37.0(±0.1) °C in 5 mm phosphate buffer (pH 6.85) with a [DNA]/[complex] ratio of 10:1.

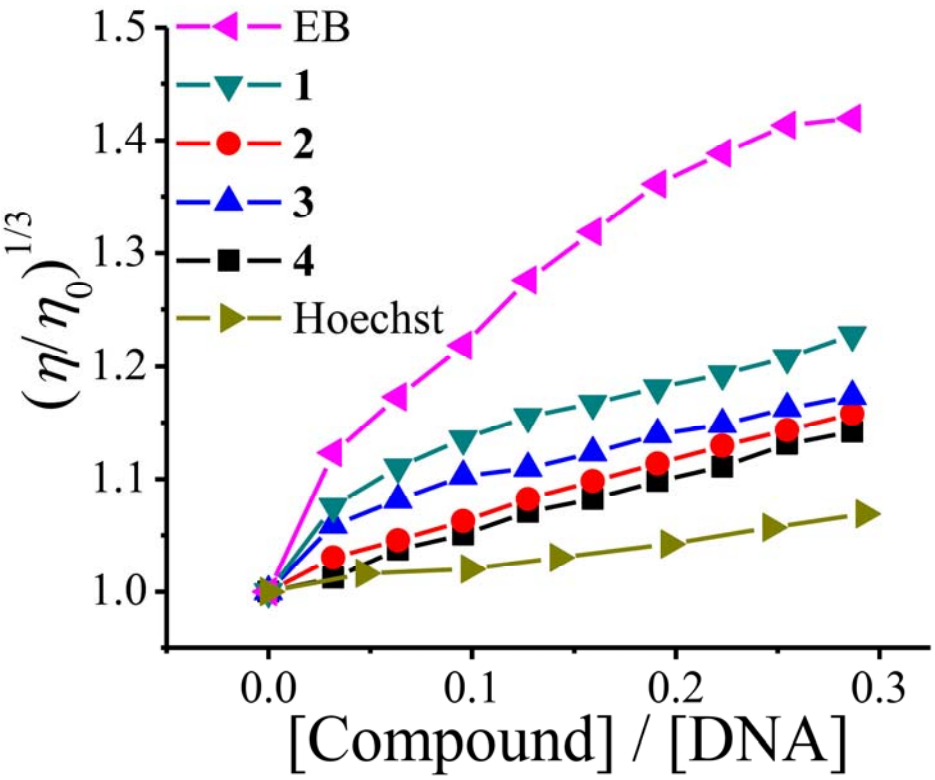

Fig. S24. Effect of increasing concentrations of the complexes **1** (▼), **2** (●), **3** (▲), **4** (■), EB (◄) and Hoechst 33258 (►) on the relative viscosities of ct-DNA at 37.0(±0.1) °C in 5 mmol Tris-HCl buffer (pH = 7.2, [DNA] = 150 μmol).

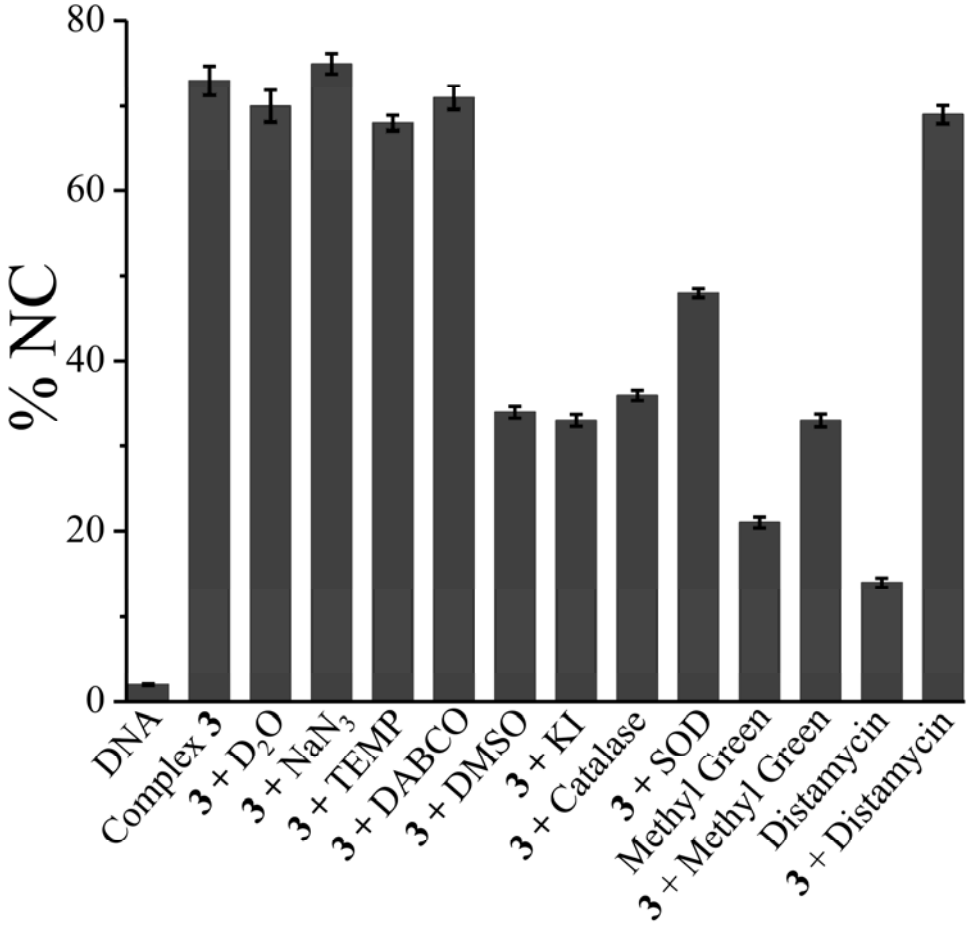

Fig. S25. Cleavage of SC pUC19 DNA (0.2 μg, 30 μmol) by the complex **3** (30 μmol) in the presence of various additives in 50 mmol Tris-HCl/NaCl buffer (pH 7.2) containing 1.5% DMF on photo-irradiation at 785 nm for 2 h. The reaction conditions are as indicated in the figure.